Catena 131 (2015) 1–13

Contents lists available at ScienceDirect

Catena

journal homepage: www.elsevier.com/locate/catena

Iron and arsenic-rich nanoprecipitates associated with clay minerals in sulfide-rich waste dumps

T. Valente [a,c,*], P. Gomes [a], M.A. Sequeira Braga [a,b], A. Dionísio [b], J. Pamplona [a], J.A. Grande [c]

[a] ICT (Institute of Earth Sciences), Pole of the University of Minho, Departamento de Ciências da Terra, Universidade do Minho, Campus de Gualtar, 4710-057 Braga, Portugal
[b] CERENA, IST, Universidade de Lisboa, Av. Rovisco Pais, 1049-001 Lisboa, Portugal
[c] CIPIMS, Centro de Investigación para la Ingeniería en Minería Sostenible, Escuela Técnica Superior de Ingeniería, Universidad de Huelva, Ctra, Palos de la Frontera, s/n. 21819 Palos de la Frontera, Huelva, Spain

ARTICLE INFO

Article history:
Received 8 October 2014
Received in revised form 6 March 2015
Accepted 14 March 2015
Available online 25 March 2015

Keywords:
Halloysite(7 Å)
Beidellite
Jarosite
Goethite
As-Fe-rich nanoparticles
Mine waste -dumps

ABSTRACT

The relationships between clay minerals and associated iron and arsenic-rich phases are a main scientific issue in reactive mine waste-dumps. Therefore, this paper documents the composition and morphology of the fine fraction (<2 μm), including the nano-sized Fe and As precipitates, associated with clay minerals in three distinctive sulfide-rich waste-dumps: *Cerdeirinha*, *Lapa Grande*, and *Penedono* (Northern Portugal).
The obtained results indicated that the study sites have similar relative proportions of the detrital materials. However, major differences were observed in the remainder phases, which is in accordance with the mineralogy that was inherited from the respective ore deposits. In general, the clay mineral assemblage is dominated by the presence of illite, halloysite(7 Å), and beidellite. There are also associated minerals, such as jarosite and goethite, as well as amorphous As-rich nanoprecipitates with specific morphologies. Moreover, the results suggested that AMD conditions control the physical–chemical transformations, namely constraining the stability of the secondary phases formed by weathering in the waste dumps. Acidity is responsible for the degradation of the clay minerals, which is reflected in their crystalochemistry, structural order–disorder, and morphology. On the contrary, jarosite is more stable, being a dominant mineral in such environmental conditions. The stability of amorphous ferric arsenates or its evolution to a more crystalline phase is dependent on the Fe:As ratio, which is lower in *Penedono*.
The study of the secondary products, especially the nanoparticles, puts in evidence their ability to control the mobility of trace elements, suggesting potential applications in environmental technology, including remediation of reactive mine waste-dumps.

1. Introduction

The occurrence of soil contamination and metal dispersion in the surrounding ecosystems is a common problem in the presence of sulfide wastes. Therefore, abandoned mine waste-dumps are often an important focus of environmental impact as the sulfide minerals are susceptible to weathering. The weathering reactions produce acid mine drainage (AMD), which is responsible for mobilizing metals, sulfate and acidity (e.g., Hoffert, 1947; Grande et al., 2010). The geochemical evolution of the sulfide wastes is typically accompanied by the development of reaction products, named AMD-precipitates. Eqs. (1) and (2) are used to simply express such mineral–water interactions, involving two common sulfides that mobilize iron and arsenic. They include the development of new mineralogical structures, here represented by the hydroxide and arsenate phases, the $Fe(OH)_{3(s)}$ and the $FeAsO_4\,2H_2O_{(s)}$, respectively.

$$\text{Pyrite}: FeS_{2(s)} + 15/4O_{2(g)} + 7/2H_2O_{(l)} \rightarrow Fe(OH)_{3(s)} + 2SO_4^{2-}(aq) + 4H^+_{(aq)} \quad (1)$$

$$\text{Arsenopyrite}: FeAsS(s) + 7/2O_{2(g)} + 3H_2O_{(l)} \rightarrow FeAsO_4 2H_2O_{(s)} + SO_4^{2-}(aq) + 2H^+_{(aq)} \quad (2)$$

The AMD-precipitates may have different compositions and nature, as they represent mild modifications or profound transformations of the primary paragenesis (Alpers et al., 2000; Valente et al., 2014). Iron oxyhydroxides and hydroxysulfates, such as schwertmannite and ferrihydrite, are among the most visible and well characterized materials in sulfide environments (Bigham, 1994; Bigham and Nordstom, 2000; Murad and Rojík, 2003). Nevertheless, the sulfide-rich wastes

* Corresponding author at: ICT (Institute of Earth Sciences), Pole of the University of Minho, Departamento de Ciências da Terra, Universidade do Minho, Campus de Gualtar, 4710-057 Braga, Portugal.
E-mail address: teresav@dct.uminho.pt (T. Valente).

http://dx.doi.org/10.1016/j.catena.2015.03.009
0341-8162/

are generally polymineralic aggregates, whose evolution is marked by other solid phases, such as sulfates, silicates (e.g., clay minerals), metallic oxides, phosphates, and arsenates. These minerals may appear simultaneously with other secondary products of very small size (in the nanometric scale) that did not realize crystalline structure (Valente and Leal Gomes, 2009a,b; Ribeiro et al., 2010). Amorphous and low crystalline precipitates are not so evident in the waste dumps and are more difficult to analyse. Therefore, they are considerably less studied AMD-precipitates. However, they have strong monitoring and environmental relevancies. Although metastable, they give valuable information concerning the composition of the solutions from which they formed as well as the prevailing equilibrium conditions on waste dumps. Furthermore, they have the ability to retain pollutants, such as arsenic, limiting the dispersion of contamination by AMD.

Another group of minerals that lacks information in AMD systems is clay minerals. Although ubiquitous, there are very few references to their interaction with other secondary minerals in AMD (Galan et al., 1999; Uzarowicz et al., 2011; Vazquez et al., 2011). However, clay minerals are key-examples of environmental minerals in accordance with the definition given by Valsami-Jones (2000). Due to their surface properties they are involved in sorption processes, retaining acidity, metals, and metalloids (Hammarstrom et al., 2003). The importance of this group of minerals in AMD is enhanced by their common association with other relevant phases, such as the oxyhydroxides and hydroxysulfates (e.g., goethite and jarosite) (Valente et al., 2012). In addition, composition and morphological modifications, induced in clay minerals by acidity, have not been studied extensively (Uzarowicz et al., 2011).

Several studies were carried out in the North of Portugal, focused particularly on the mineralogy and geochemistry of AMD systems (Valente et al., 2011, 2012). Also, Gomes et al. (2013) present the composition and role of clay minerals, when studying the restoration promoted by natural vegetation in distinct mine waste-dumps. Though, these studies need to be complemented, in order to describe the variety of very fine-grained products that intimately occur in sulfide waste-dumps: clay minerals, goethite, jarosite, and nanoprecipitates (defined as < 100 nm in size) that often occur without crystallinity.

Recent advances have shown the key role that the fine fraction, especially the nanoparticles, plays in aqueous and soil systems (Waychunas et al., 2005; Plathe et al., 2013). Their ability to control the mobility of trace elements may suggest important applications in environmental technology, including remediation of reactive mine waste-dumps.

This paper documents the composition and morphology of the fine fraction (<2 μm), including the small-sized Fe and As precipitates, associated with clay minerals. Three sulfide-rich waste-dumps in the North of Portugal were used to represent distinctive AMD environments. The following aims were defined: i) to characterize the mineralogy and geochemistry of clay minerals that prevail at each site; ii) to understand the behaviour of kaolin minerals, smectite, and associated minerals (jarosite and goethite) in distinctive AMD environments; and iii) to describe the morphological and compositional properties of the iron and arsenic-rich nanoprecipitates.

2. Materials and methods

2.1. Study sites

The three studied sites, *Cerdeirinha*, *Lapa Grande* and *Penedono*, are located in the North of Portugal (Fig. 1), which is a region with a long and large mining tradition. *Cerdeirinha* and *Lapa Grande* (in Northwest of Portugal) resulted from the exploitation of wolframite and scheelite in a skarn ore deposit with abundant pyrrhotite and pyrite (Valente and Leal Gomes, 2007). Although similar, these two waste dumps differ on the proportion of sulfides relatively to other minerals with neutralizing potential (calcite, apatite and Ca-silicates) and on the granularity of the wastes. At *Cerdeirinha*, silt and clay dimensions prevail and the wastes are more enriched in sulfides.

Penedono, a hydrothermal deposit, is located in the Northeast of Portugal (Fig. 1) and the waste dumps resulted from the exploitation of gold in quartz veins with sulfides, associated with second order shear zones (Silva and Neiva, 1990). The waste dumps are composed by small grain size tails, which resulted from milling, hydrogravitic separation and flotation. The inherited mineralogy that characterizes the mine wastes is rather monotone, with high proportion of arsenopyrite and Al-silicates (Valente et al., 2012). Neutralizing phases, such as carbonates, are absent.

2.2. Sampling and preparation procedures

Sampling of the three mine soils took place between January and June 2011. Six to eight samples were randomly collected at each waste dump. On the whole, the sampling sites represent the diversity of topographic, microclimatic, and mineralogical conditions. Their location was also affected by the difficulty to access some of the areas, due steep slopes and strong erosion that disturb, especially, *Lapa Grande* and *Penedono*. At each sampling site, a pooled sample was obtained for a 20 cm soil depth from a circular area of 50 cm. Once the samples arrived at the laboratory, they were dried at 40 °C for 72 h and sieved through a 2 mm steel sieve.

2.3. Analytical methods

The samples from the <2 μm fraction were analysed for chemistry and mineralogy. Chemical composition was obtained by inductively-coupled plasma mass spectrometry (ICP-MS) after an *Aqua Regia* extraction for the following elements: Fe, As, Mn, S, P, Na, K, and Al. These analyses were performed at Activation Laboratory, Lda (Actlabs, Canada), including duplicate samples and check precision blanks, whereas accuracy was obtained by using certified standards (GXR series). Also, soil pH was analysed on extracts obtained in accordance with Wilke (2005).

The mineralogy of the samples was analysed by X-ray powder diffraction (XRD) with a Philips X'pert Pro-MPD diffractometer (Philips PW 1710, APD), using CuKα radiation. The diffractometer is provided with automatic divergence slit and graphite monochromator. The XRD diffractograms were obtained from powders (bulk sample <2 mm as well as the <2 μm fraction) and from oriented aggregates (<2 μm fraction) in the interval of 3 to 65°2θ and 3 to 35°2θ, respectively. The equipment was operated with a 2θ step size of 0.02° and a counting time of 1.25 s.

Prior to analysis, the bulk samples were air-dried and sieved to <2 mm grain size and then crushed and ground manually using an agate mortar and pestle. For the separation of the <2 μm fraction, organic matter was previously removed by treating samples with H_2O_2 *p.a.* This treatment was applied to the samples which are more enriched in organic matter, in order to obtain a full dispersion of the clay minerals. The <2 μm fraction was then obtained by the sedimentation method and the particle-size separation based on Stokes' law. The oriented preparations were submitted to the following treatments: air-dried, ethylene glycol (EG)-solvated, and heated (490 °C). Li saturation (LiCl), heat treatment (300 °C) and ethylene glycol saturation were also applied. Oriented mounts of the <2 μm fraction on opaque fused silica slide were analysed by XRD according with the Greene-Kelly test (Greene-Kelly, 1952; 1953).

Semi-quantitative analysis on bulk samples was performed by using the peak-height intensities of the diagnostic reflections (Valente et al., 2012). Estimation of the clay minerals was deduced from the diagnostic peaks related to their first-order basal reflections in air-dried conditions or after EG solvation.

Fourier Transform Infrared (FTIR) spectroscopy was applied to the <2 μm fraction, using a Perkin Elmer Spectrum 65 spectrometer for

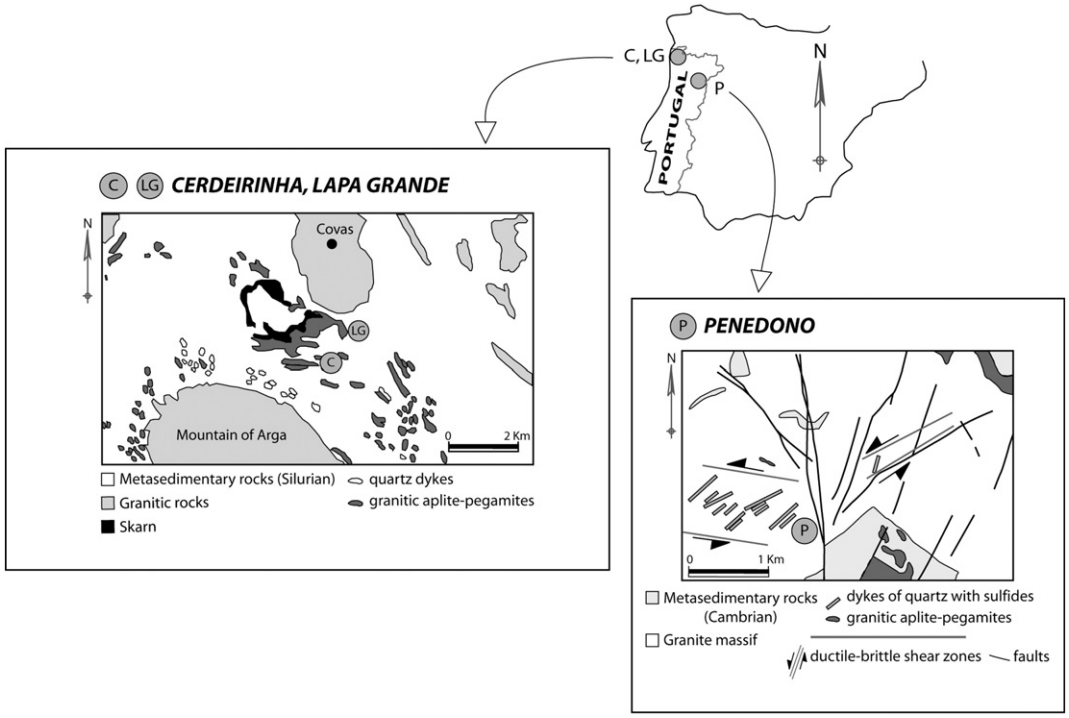

Fig. 1. Geological maps with the location of the three mine waste-dumps. Adapted from Valente et al. (2012).

samples dried at 70 °C. Powdered samples were dispersed in KBr pellets and IR spectra were recorded for the 4000 cm^{-1} to 400 cm^{-1} region.

In addition, mineralogical study was performed by transmission electron microscopy (TEM) coupled with EDS equipment. Selected area electron diffraction (SAED) was used to provide crystallographic information from sub-micron regions of the samples. These analyses were carried out with a Hitachi 8100 microscope coupled with a ThermoNoran EDS detector for light elements. The clay fraction was dispersed using ultrasonics, then diluted and a holey carbon-coated copper grid, having a diameter of the inner mesh area of ~2.5 mm, was dipped in the diluted sample and allowed to air dry. The 200 mesh copper grid was placed into the sample holder, which was attached to the specimen stage. Field emission scanning electron microscopy (FESEM) was performed using a FESEM Jeol JSM-7001F microscope, equipped with an Oxford EDS light element detector at an acceleration voltage of 15 kV. Semi-quantitative microanalysis and characterization of mineralogical phases were carried out on rock fragments, previously coated with a thin carbon film. Some samples were analysed by SEM (on gold coated samples) with a LEICA S360 microscope, combined with an energy dispersive system (SEM-EDS).

3. Results

3.1. Chemistry

The pH and chemical composition of the samples of the <2 μm fraction are given in Table 1. The pH values are identical for the three sites, varying in the acidic range, with the lowest value in *Lapa Grande* (average pH of 3.4).

The most abundant element is iron (Table 1). *Cerdeirinha* presents the highest average values for Fe (17.6%), Al (6.00%) and S (1.76%), whereas *Lapa Grande* shows the highest mean concentration for P (1.17%). Fe and As are the most abundant elements in *Penedono* (12.2 and 2.59%, respectively), whereas Al, S, P, and Mn are present in low amounts, comparatively with the other waste dumps. All the analysed samples are characterized by small contents in Mg, Na, Ca, and K.

3.2. XRD

The semi-quantitative mineralogical composition estimated by XRD in the <2 mm fraction is presented in Table 2. Among the detrital materials, quartz is the most abundant mineral in all the samples. The other detrital minerals are present in low amounts and clay minerals occur in vestigial proportions (≤3%). The sulfides are represented by pyrite, marcasite and pyrrhotite in *Lapa Grande* and *Cerdeirinha*. In addition, Table 2 reveals the presence of iron-oxyhydroxides (goethite) and hydroxysulfates (jarosite). These minerals appear in vestigial amounts (≤4%). In *Penedono*, the XRD results obtained for this fraction revealed only the relevant presence of detrital minerals. Clay minerals and jarosite were identified in trace amounts.

The clay sized fraction (<2 μm) is characterized, in general, by clay minerals (chlorite, illite, mixed-layer mica–vermiculite (M–V), smectite and kaolin minerals) and associated minerals (goethite, jarosite and gibbsite) (Table 3). At *Penedono*, the most abundant clay minerals, considering average proportions, are kaolin mineral (39%) and illite (20%), followed by smectite (15%). At *Lapa Grande*, kaolin mineral is also dominant (27%) followed by smectite (11%). At *Cerdeirinha*, kaolin mineral and smectite are also present, but in lower amounts.

Considering the associated minerals, jarosite is ubiquitous in the three sites. It is present in considerable amounts (Table 3): average values of 40%, 55% and 27%, in *Lapa Grande*, *Cerdeirinha* and *Penedono*, respectively. Goethite is also relevant, especially in the *Lapa Grande* samples, whereas at *Penedono* it appears only in trace amounts.

Chlorite was identified by 00 *l* reflections (002, 003, 004, 005) as recommended by Moore and Reynolds (1997). In fact, the reflections centred at 7 Å, 4.72 Å, 3.54 Å and 2.81 Å indicate the presence of chlorite (Fig. 2a and c). The XRD patterns in the random powder mounts (Fig. 2b and d) show the di-trioctahedral character of the chlorite by the d_{060} reflections at 1.543–1.546 Å.

Table 1
Average and range values of pH, metals and arsenic in the <2 μm fraction. LG — *Lapa Grande*; C — *Cerdeirinha*; P — *Penedono*.

Waste-dump	Soil pH (KCl)	%										
		Al	Na	Ca	Mg	K	S	P	Fe	As	Mn
LG (n = 7)	3.4	3.83	0.048	0.620	0.220	0.320	1.32	1.17	14.1	0.260	0.140
	(2.8–3.8)	(2.74–4.68)	(0.030–0.090)	(0.250–1.44)	(0.140–0.290)	(0.110–0.830)	(0.360–4.21)	(0.750–2.00)	(10.4–20.3)	(0.050–1.00)	(0.020–0.370)
C (n = 6)	3.9	6.00	0.190	0.78	0.220	0.520	1.76	0.970	17.6	0.410	0.062
	(3.4–4.1)	(4.06–7.98)	(0.070–0.370)	(0.460–1.22)	(0.110–0.310)	(0.240–0.790)	(0.470–4.07)	(0.790–1.28)	(11.9–21.9)	(0.280–0.600)	(0.032–0.094)
P (n = 8)	3.6	1.10	0.039	0.050	0.039	0.160	0.140	0.500	12.2	2.59	0.006
	(3.2–4.3)	(0.57–3.77)	(0.030–0.060)	(0.000–0.230)	(0.030–0.090)	(0.100–0.240)	(0.030–0.300)	(0.070–1.07)	(5.15–18.5)	(1.24–4.05)	(0.001–0.028)

In the oriented and non-oriented samples, the main reflections for illite, in all sites, are the 001, 002 and 003, although other peaks can be identified (Figs. 2 and 3). The overlapping of the basal reflections of illite with peaks of other clay minerals (e.g., smectite) and non-clay minerals (e.g., quartz) provides interferences on the behaviour of the XRD profiles. So, this is an important factor in the difficulty of the illite characterization. Nevertheless, values for d_{001} of 10.1 Å and d_{002} of 5.02–5.03 Å, which are not influenced by EG-solvated conditions, indicate the presence of illite.

Fig. 2c shows a small broad shoulder approximately between 8.8°2θ and 4.1°2θ (CuKα radiation), which suggests the presence of a mixed-layer (Moore and Reynolds, 1997). A broad and weak peak approximately at 12 Å that coexists in both untreated (air-dried) and EG-solvated samples and which collapsed down to 9.9–10 Å upon heating at 490 °C, supports the supposition of an irregular mixed-layer M–V.

Smectite was identified by a broad reflection in all the studied samples to the low-2θ regions centred at 14 Å. Depending on the waste-dump sites, the basal spacing show slight differences, concerning the smectite features. In *Lapa Grande* and *Cerdeirinha* the d_{001} values, in the air-dried samples, range between 13.2 and 14.7 Å and 14.1 and 14.7 Å, respectively (Fig. 2a and c). In *Penedono*, the basal spacing ranges between 12.2 Å and 13.8 Å (Fig. 3a). In the EG-solvated conditions, for all sites, the position of the 001 reflection expanded to approximately 17 Å. In some samples, a second order reflection at 8.6 Å occurs. After heating until 490 °C, the peak at 17 Å collapses to 10 Å (Figs. 2a, c and 3a). Such behaviour is characteristic of smectite and the XRD patterns show its low-degree of order. Moreover, in the random powder mounts the 61.30–62.20°2θ region is dominated by a broad reflection centred at 1.49–1.50 Å (Figs. 2b, c and 3b). The position and shape of the 06,33 reflection at 1.506–1.51 Å is ascribed to a dioctahedral smectite, pointing to either montmorillonite or beidellite (Moore and Reynolds, 1997). However, the Greene-Kelly test (Greene-Kelly, 1953) confirmed the presence of beidellite in the three sites. This dioctahedral character is also ascribed to other 2:1 minerals (illite and mixed-layer M–V), while the 060 reflection at 1.49 Å indicates the presence of 1:1 minerals, such as kaolin mineral.

Figs. 2 and 3 present typical XRD patterns of the oriented <2 μm. The presence of the kaolin mineral was detected by their d_{001} and d_{002} reflections centred at 7.10–7.21 Å and 3.58 Å. At *Lapa Grande* the XRD pattern (Fig. 2a) is quite different from *Cerdeirinha* (Fig. 2c), being less sharp and intense for the *Cerdeirinha* samples, indicating an increasing disorder (Brindley, 1980). In *Penedono*, kaolin mineral is characterized by sharp basal peaks (d_{001} and d_{002}) at 7.18 Å and 3.58 Å (Fig. 3a). Besides, the 001 reflection has a slight asymmetry at the low-angle side. Comparing the 00 *l* and *hk* indices and respective *d* values of the studied XRD patterns with data for halloysite from Brindley (1980), the kaolin mineral can be ascribed to halloysite(7 Å). In fact, regarding the random XRD pattern in Fig. 3c, the 00 *l* peaks are relatively weak, and the non-basal reflections (*hk* indices) are strong at about 20°2θ and 35°2θ (Moore and Reynolds, 1997).

Among the non-clay minerals, the most significant phase is jarosite. It was identified in the oriented <2 μm fraction by the most important reflections at ~3.08 Å and ~3.11 Å, together with the series of reflections (Fig. 2a and c) given by Brindley and Brown (1980). Generally, the XRD patterns show symmetric and sharp reflections (Fig. 2c) indicating the presence of jarosite with high degree of order. Goethite was the iron oxyhydroxide that was identified in these assemblages. Its appearance is accompanied by broad and weak diffraction peaks at 4.16–4.18 Å and 2.69–2.70 Å. The large shape of the peaks and their low intensity suggest the presence of poorly crystallized goethite.

3.3. FTIR

Fig. 4 shows the results of FTIR analyses performed for *Lapa Grande* and *Penedono* samples. The spectra confirm the presence of beidellite, halloysite and jarosite. Beidellite was assigned by the presence of OH-

Table 2
Semi-quantitative mineralogical composition of the samples estimated by XRD in the <2 mm size fraction. Q = quartz; F = k-feldspar; P = plagioclase; Mi = mica; Cm = clay minerals; Py = pyrite; Mar = marcasite; Pyr = pyrrhotite; Go = goethite; Jt = jarosite; Si = Siderite; Mgs = magnesite; Ap = apatite; Am = amphibole; Wo = wollastonite; Al = alunite; tr = vestigial.

Waste dumps	Sample code	<2 mm fraction (%)															
		Q	F	P	Mi	Cm	Py	Mar	Pyr	Go	Jt	Si	Mgs	Ap	Am	Wo	Al
Lapa Grande	LG1	46	–	12	8	3	6	8	–	3	4	5	–	5	–	–	–
	LG2	60	2	3	10	3	2	3	–	3	3	4	–	5	–	–	2
	LG3	44	–	9	15	3	1	5	4	4	2	6	–	5	–	–	2
	LG4	55	2	4	10	3	2	3	2	4	3	4	–	4	–	–	4
	LG5	60	2	1	5	2	2	6	14	2	–	2	–	4	–	–	–
	LG6.1	57	4	2	23	1	1	1	4	1	1	3	–	2	–	–	tr
	LG6.2	51	3	18	6	2	2	3	2	2	2	4	–	4	–	–	1
Cerdeirinha	C1	54	3	16	6	1	1	–	10	1	3	–	–	3	1	1	–
	C2	29	26	5	9	1	1	9	1	1	2	–	10	4	tr	2	–
	C3	77	3	3	8	tr	tr	1	1	1	1	–	2	1	1	1	–
	C4	44	4	4	5	1	6	6	6	2	2	–	10	9	tr	1	–
	C5	45	13	14	3	1	2	7	3	2	2	–	5	2	tr	1	–
	C6	47	2	9	3	1	3	13	6	2	3	–	5	4	2	–	–
Penedono	P1	90	2	4	4	tr	–	–	–	–	–	–	–	–	–	–	–
	P2	90	5	1	4	tr	–	–	–	–	tr	–	–	–	–	–	–
	P3	89	5	3	3	tr	–	–	–	–	–	–	–	–	–	–	–
	P4	82	12	12	4	tr	–	–	–	–	–	–	–	–	–	–	–
	P5	68	5	13	14	tr	–	–	–	–	–	–	–	–	–	–	–
	P6	87	4	6	3	tr	–	–	–	–	–	–	–	–	–	–	–
	P7	84	7	4	4	1	–	–	–	–	–	–	–	–	–	–	–
	P8	92	5	1	2	tr	–	–	–	–	–	–	–	–	–	–	–

stretching frequency at 3651 cm^{-1} and vibration bands centred at 1032–1035, 914, 526–538, and 470 cm^{-1} (Fig. 4a and b). Similar bands were reported by Russell and Fraser (1994) and Kloprogge (2006). Moreover, the presence of beidellite is corroborated by the absence of the 630 cm^{-1} band (Dill et al., 2011).

The presence of OH-stretching frequencies at 3694–3697 and 3621 cm^{-1} and vibration bands centred at 1032–1035, 1009–1012, 914, 796–799, 754, 695, 538, 470, and 431–434 cm^{-1} (Russell and Fraser, 1994) allowed the identification of halloysite.

Band assignments for vibrational features in jarosite (Fig. 4b) are in agreement with Bishop and Murad (2005): 3393, 1181, 1080, 1009, and 470 cm^{-1}. The sample in that figure contains some quartz impurity (vibration bands centred at 1080, 799, 782, 695, and 470 cm^{-1}).

Table 3
Semi-quantitative mineralogical composition of the samples estimated by XRD in the <2 μm fraction (clay minerals and associated minerals). C = chlorite; Il = illite; M–V = mixed-layer mica–vermiculite; Sm = smectite; K = kaolin mineral; Go = goethite; Jt = jarosite; Gi = gibbsite; tr = vestigial.

Waste dumps	Sample code	<2 μm fraction							
		C	Il	M–V	Sm	K	Go	Jt	Gi
Lapa Grande	LG1	–	2	1	3	5	2	87	–
	LG2	–	19	–	7	18	10	46	–
	LG3	6	4	–	5	26	14	45	–
	LG4	3	5	–	12	25	12	38	5
	LG5	2	4	–	16	36	16	22	4
	LG6.1	3	3	–	20	40	15	15	4
	LG6.2	tr	3	–	16	40	13	28	–
Cerdeirinha	C1	1	4	–	3	8	9	76	–
	C2	tr	2	tr	3	2	–	93	–
	C3	3	16	15	–	13	8	23	18
	C4	8	6	14	9	tr	21	26	16
	C5	7	4	7	10	9	15	43	5
	C6	2	1	–	9	9	8	71	–
Pedendono	P1	–	13	–	9	28	tr	50	–
	P2	–	5	–	3	60	tr	32	–
	P3	–	19	–	24	15	tr	42	–
	P4	–	31	–	18	51	tr	–	–
	P5	–	22	–	29	32	2	11	4
	P6	–	22	–	19	59	tr	tr	–
	P7	–	19	–	12	43	–	26	–
	P8	–	14	–	9	25	tr	52	–

3.4. TEM

The mineralogical study based on TEM observations, accompanying SAED patterns, was focused on crystal morphology and chemical composition of clay minerals (beidellite and halloysite(7 Å)) and associated phases (jarosite, goethite and As–Fe-rich nanoparticles).

This study, accomplished on <2 μm fraction, revealed that clay minerals are similar in morphology and composition in the three studied waste dumps. Beidellite crystals show irregular anhedral morphology. They occur as platelets, which tend to form very thin films, with a veil-like smectite texture. This texture shows especially curled edges (Figs. 5a and 8e). Also, bent beidellite flakes occur with random orientation (Fig. 5b). SAED pattern (inset) in Fig. 5a establishes the poorly crystalline nature of beidellite by their weak, broad rings at ~3.97 Å and ~2.25 Å. In addition, the broad diffuse rings at ~3.97 Å and ~3.18 Å spacing, measured in SAED pattern (Fig. 6b), are consistent with beidellite. TEM-EDS spectra obtained on beidellite platelets indicate similar composition, marked by low Si:Al ratio (Figs. 5c, d and 8g). Some samples revealed also the presence of Mn and Fe (Fig. 5d) or Mg and Fe (Fig. 8g), but in small amounts.

Halloysite was the only kaolin mineral identified, which was confirmed by its tubular morphology, as observed in Figs. 5, 6, and 7. TEM analysis indicates considerable variations (e.g., Fig. 5a): their ends are enrolled or, in same cases more slender tubules emerge from the larger ones, as it was referred by Henning and Störr (1986). The length of the tubes varies between 7 nm and 16.4 nm, while the diameter is in the interval of 17 to 191 nm.

Jarosite exhibits well defined euhedral habits, including hexagonal (Fig. 7a) and pseudohexagonal (e.g., Fig. 7b) crystals. The former ones were observed at the three waste dumps and occur in a small range of sizes (maximum dimensions between 2 and 7 nm). The EDS analysis yields the corresponding high peaks of S and Fe and the smaller one of K (Fig. 7e). Besides, at *Penedono* jarosite often revealed the presence of arsenic (not shown). Fig. 7b shows the textural relationship between jarosite and beidellite.

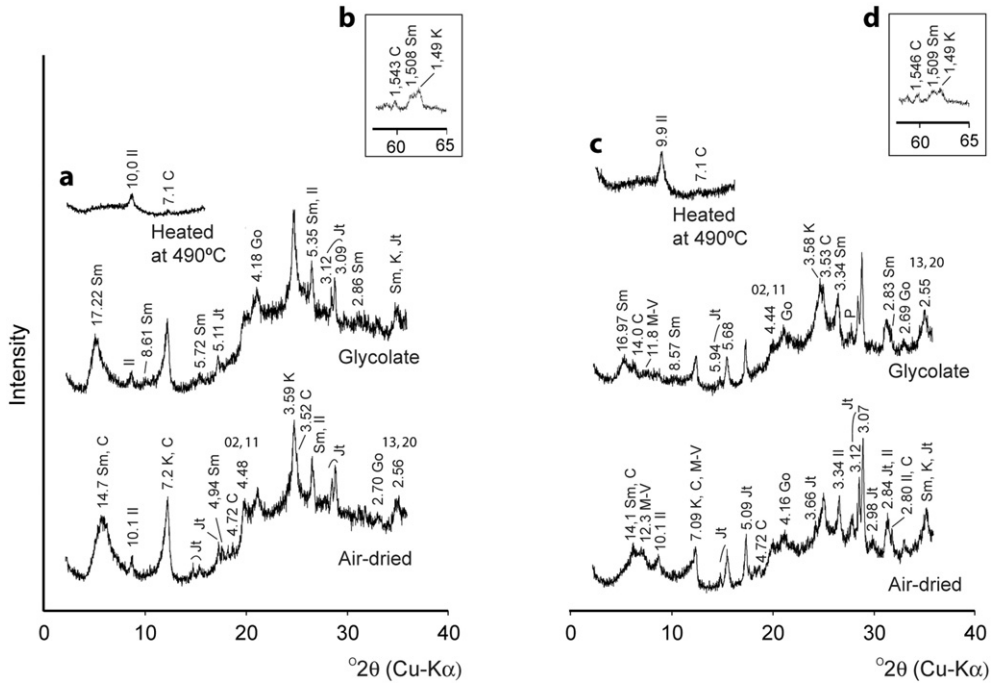

Fig. 2. Oriented mount XRD patterns showing *d* values (Å) of the <2 μm fraction for (a) LG5 sample (*Lapa Grande*) and (c) C5 sample (*Cerdeirinha*); (b) and (d) random power mounts showing d_{060} values of smectite (Sm), kaolin mineral (K) and chlorite (C) for LG5 and C5 samples, respectively. P = plagioclase; Il = illite; M–V = mixed-layer mica–vermiculite; Jt = jarosite; Go = goethite.

Goethite in samples from *Cerdeirinha* and *Lapa Grande* is identical in morphology. This goethite appears often as aggregates with acicular, needles and globular habits, as described below:

(i) very fine acicular crystals randomly scattered in beidellite platelets, as shown in Fig. 5b;
(ii) spherical nanoparticles (Fig. 6b) lined and overlapping the beidellite platelets; the particle size ranges from ~0.3 to 12 nm in diameter;
(iii) entwined needles of goethite admixture with halloysite and beidellite as illustrated in Fig. 6c;
(iv) aggregates of lath-shaped crystals, showing some trend to form stellated intergrowths (not shown);
(v) acicular or lath-shaped crystals (Fig. 6d) forming rafts as named by Landers et al. (2009) over beidellite platelets.

The morphologies referred above (item iv and v) range in length up to ~70–330 nm and in width up to ~25–165 nm. SAED patterns of acicular crystals confirm the identification of goethite (Figs. 5b and 6b). SAED measures in Fig. 5b (inset), allowed to identify goethite by their diffuse diffraction rings around the *d*-spacing at 4.13–2.64–1.81

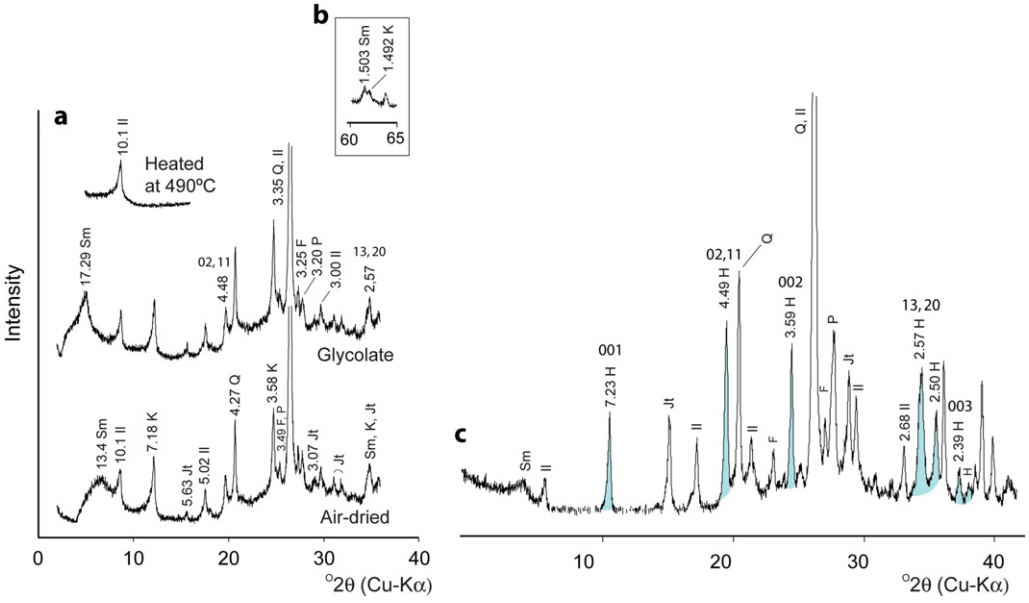

Fig. 3. XRD patterns of <2 μm fraction for P5 sample (*Penedono*). (a) Oriented mounts showing *d* values (Å); (b) random powder mounts showing d_{060} values of smectite (Sm) and kaolin mineral (K); (c) random XRD pattern of the halloysite(7 Å) (H) (highlighted blue peaks). Il = illite; Jt = jarosite; Q = quartz; F = K-feldspar; P = plagioclase.

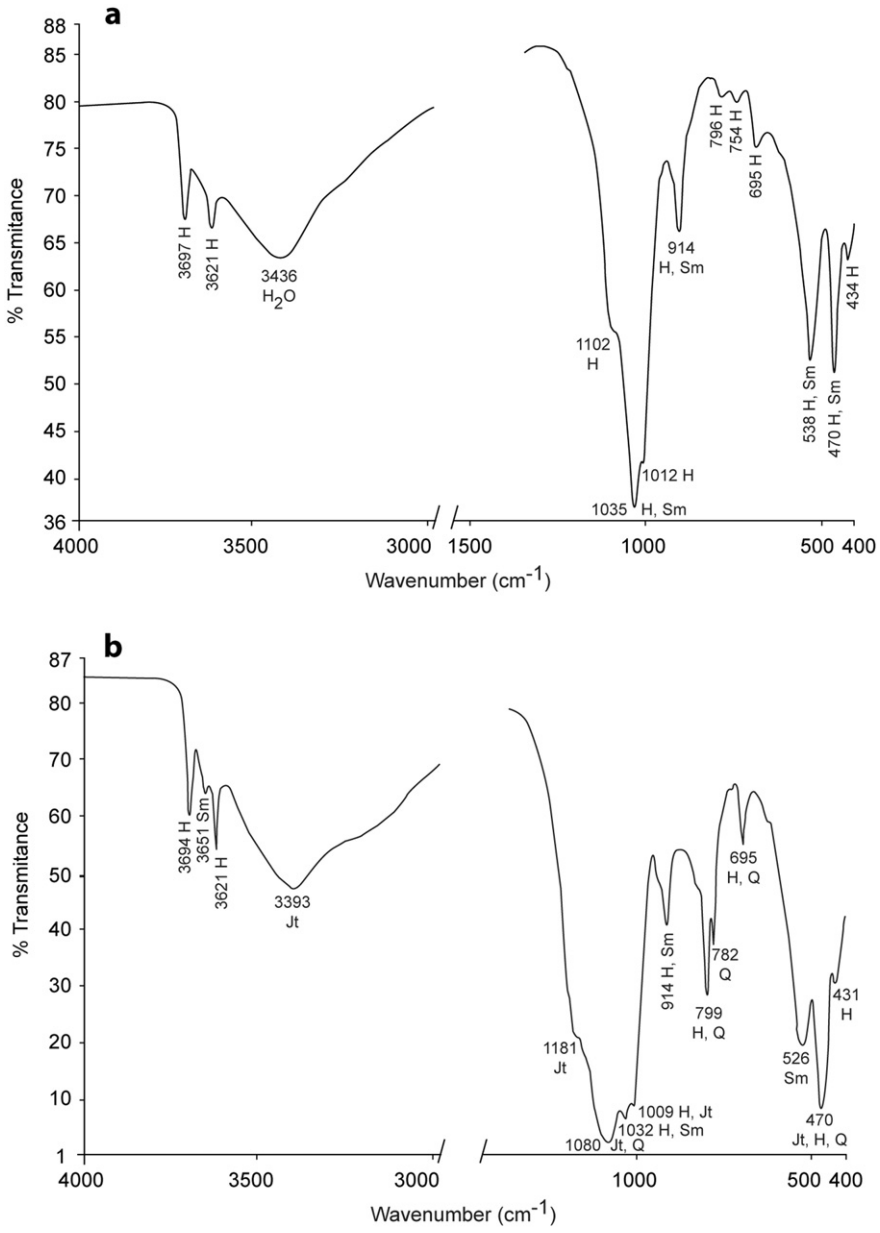

Fig. 4. Infrared spectra of <2 μm fraction for (a) LG6.1 sample (*Lapa Grande*) and (b) P2 sample (*Penedono*). H = halloysite; Sm = smectite; Jt = jarosite; Q = quartz.

and 1.72 Å. Fig. 6b (inset) shows that goethite nanoparticles coexist with beidellite. Measures of weak dots at ~2.40 Å and ~2.19 Å also correspond to goethite *d*-spacing. At *Penedono*, goethite defines only one type of morphology represented by aggregates of spherical nanoparticles (Fig. 8a) with diameters around 30 to 70 nm. SAED patterns of poorly crystalline goethite present *d*-spacing at 4.11–2.40–1.35 and 1.15 Å (Fig. 8b); EDS analyses (Fig. 8d) indicate the presence of arsenic associated with these nanoparticles.

In addition to this goethite, other morphologies were detected:

(i) spherical particles as observed at *Lapa Grande* (e.g., Fig. 7c and d), *Cerdeirnha* and *Penedono*, with average diameter in the interval of ~4–180 nm. The EDS analyses revealed always the presence of arsenic and iron (Fig. 7f). Some of these particles have richer iron halo (Fig. 7d).

(ii) Clusters of particles with granular texture and irregular edges at *Penedono* (e.g., Fig. 8a and e). The EDS spectrum revealed the presence of arsenic and iron (Fig. 8f). These clusters are generally associated with beidellite (Fig. 8e and g).

In general, a remarkable association between clays and non-clay minerals, particularly jarosite (Fig. 7a, b and c), Fe-oxyhydroxides (Figs. 5b, 6c, d and 8a) and Fe–As-rich nanoparticles (Figs. 7c, d; 8a and e), is observed. TEM analyses performed on very thin beidellite platelets confirmed their association with the iron-oxyhydroxides.

3.5. FESEM and SEM-EDS

Observations by electron microscopy were focused on the study of jarosite and goethite crystal habits as well as of other secondary phases. FESEM study performed on rock fragments indicates that jarosite, in *Cerdeirinha*, appears with pseudocubic habit (Fig. 9a) showing high

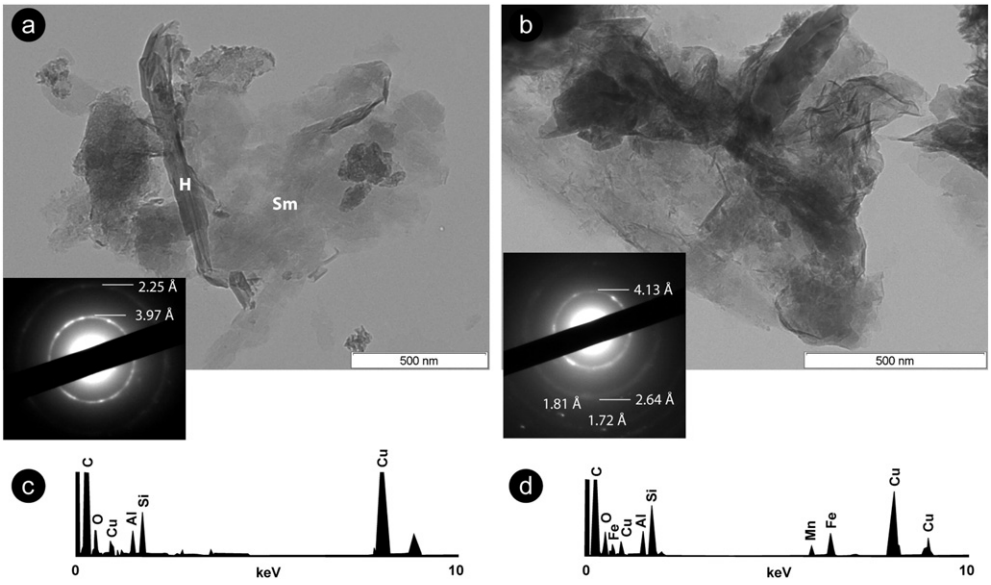

Fig. 5. TEM images of *Lapa Grande* sample with beidellite particles (a) and mix of beidellite and random needles of goethite (b); SAED patterns (inset) with *d*-spacings for beidellite (a) and for goethite (b); EDS spectra of the beidellite particles (c–d). H = halloysite; Sm = smectite.

crystalline character. These crystals have a size of ≤15 nm. It must also be noted the occurrence of dissolution features at the crystal edges.

Regarding texture relations, Fig. 9a shows the deposition of jarosite aggregates upon a goethite coating. Goethite appears as radiating individual rod-shaped particles (Fig. 9b), which developed terminations like iron-rich spherical nodules. The nanoparticles of goethite are generally coating the cleavage planes or faces of primary minerals (Fig. 9a).

Jarosite always coexists with goethite and As–Fe-rich nanoparticles as well as with clay minerals, particularly halloysite. Chemical spectra

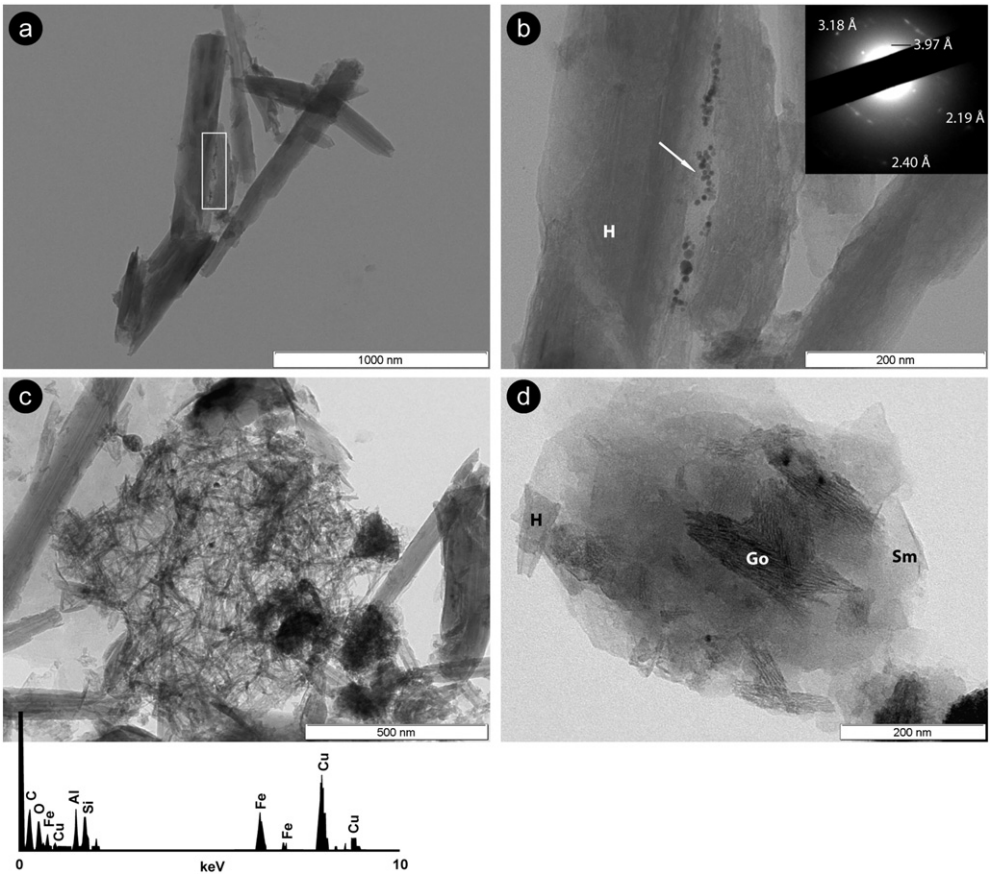

Fig. 6. TEM images of *Cerdeirinha* sample with halloysite tubes (a) and goethite spherical nanoparticles, in the area marked in (a), overlapping beidellite platelets observed at the higher magnitude (b); the SAED pattern (inset) indicates a mix of beidellite and goethite (b); aggregate of goethite needles overlapping beidellite platelets and halloysite tubes (c); EDS spectrum of goethite contaminated by chemical spectrum of halloysite (c); rafts of acicular goethite crystals over beidellite platelets (d). H = halloysite, Go = goethite; Sm = smectite.

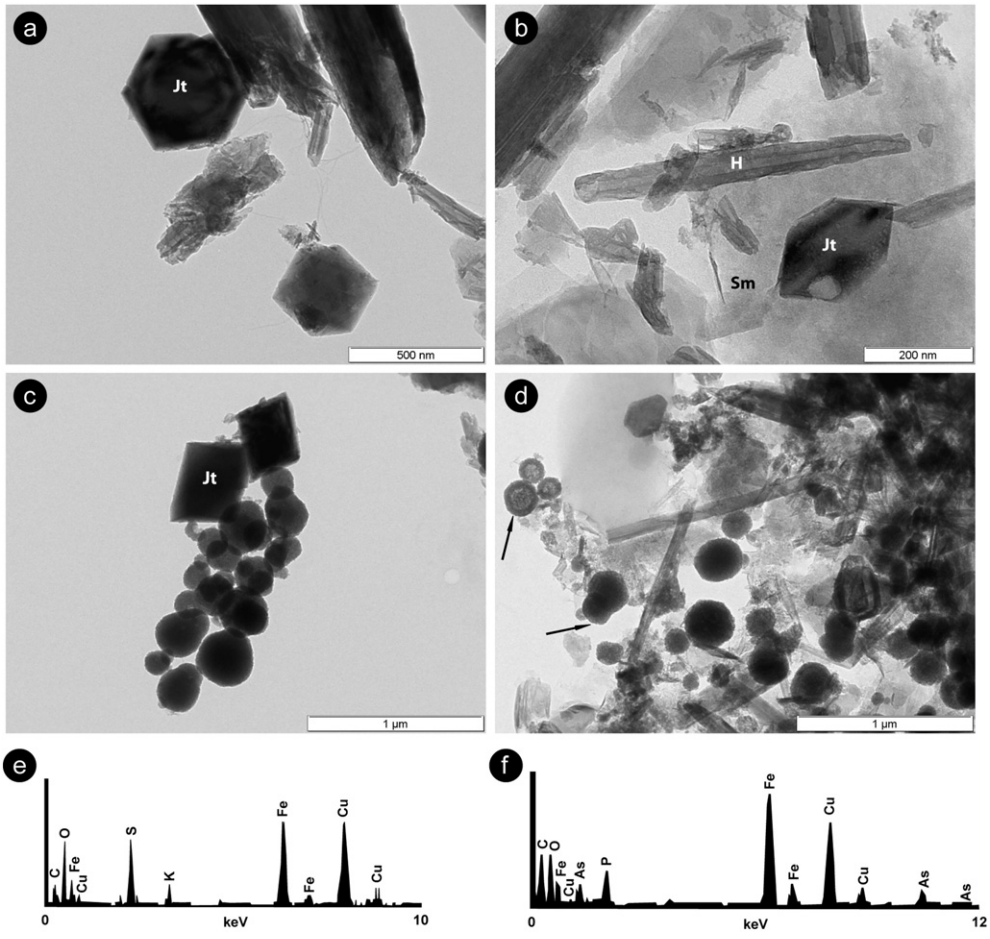

Fig. 7. TEM images of two hexagonal crystals of jarosite from *Lapa Grande* surrounded by halloysite and tiny acicular goethite crystals (a); euhedral jarosite from *Cerdeirinha* embedded in beidellite (b); rhombohedral looking jarosite crystals from *Lapa Grande* associated with spherical nanoparticles (c); clay minerals assemblage in close association with Fe–P–As-rich spherical nanoparticles (d). EDS spectrum of jarosite obtained from the upper hexagon (a–e); EDS spectrum of spherical nanoparticles (d–f); H = halloysite; Sm = smectite; Jt = jarosite.

of jarosite (Fig. 9d) from *Cerdeirinha* yielded the presence of As and P. Also, this chemical spectrum shows the presence of elements from the clay mineral composition.

SEM-EDS (Fig. 9c) of samples from *Penedono* show spherical particles with a pincushion aspect. Such aggregates, which lack crystallinity as determined by XRD and TEM, are mainly composed by arsenic and iron (Fig. 9e).

4. Discussion

4.1. Clay minerals

At *Lapa Grande* and *Cerdeirinha*, chlorite is an inherited mineral from the skarn deposits, which explains its presence at both waste dumps. On the contrary, at *Penedono* chlorite is absent, and, in accordance with the local geology, the clay fraction is dominated by kaolin minerals and illite (Table 3).

The XRD patterns (Fig. 3) of kaolin minerals are ascribed to halloysite(7 Å), which was corroborated by the TEM-EDS study. In fact, the typical tubes of halloysite are ubiquitous in the samples from the three sites. However, this tubular morphology shows distinct variations in the rolling of the layers (Figs. 5, 6 and 7). The apparent splitting and partial or complete collapse of the halloysite(7 Å) tubes were frequently observed, similarly to the study of Bates (1971) for mining soils. A possible explanation for such morphological variations may be the cycling of dehydration processes that occur in the waste dumps.

Regarding smectite, the data obtained by TEM-EDS show a consistently low Si:Al ratio. Such a low Si proportion may be either due to high substitution of the Si^{4+} for tetrahedral Al^{IV}, or Al^{VI} is the prevailing octahedral cation. Although in small amounts, Mn and Fe or Mg and Fe also appear in the smectite spectra. These features are in agreement with the chemistry of the mine wastes presented in Table 1: (*i*) high contents of Al and Fe; (*ii*) low amounts of Mg and alkalis. The high peak of Fe that was observed in several spectra may be due to the overlapping of very fine acicular crystals of goethite on smectite platelets (Fig. 5b and d). So, chemical data do not reveal the presence of a true smectite phase composition. A possible reason for that is the lack of alkali elements (Na, Ca, K) in the smectite interlayer. This may be justified by the high acidity conditions, which promote leaching of the alkali elements. These chemical features do not have mineralogical meaning in terms of atoms per unit formula and, simultaneously, point out to the presence of an Al-dioctahedral smectite. The dioctahedral composition of these 2:1 clay minerals is in agreement with the d_{060} values obtained by DRX (Figs. 2 and 3). So, combining the XRD and compositional data with SAED patterns it is possible to suggest that the analysed smectite is in the domain of beidellite. In fact, Fig. 5a and b shows the diffuse diffraction rings with beidellite *d* values, around 3.97 Å and 2.25 Å.

Moreover, the results of the diagnostic Greene-Kelly test indicate the presence of beidellite. Additionally, infrared spectroscopy (FTIR) was a valuable tool for distinguishing montmorillonite from beidellite. Indeed FTIR has been for decades a frequently used method to investigate the structure, bonding and chemical properties of clay minerals (Russell and Fraser, 1994; Dill et al., 2011). In this specific case, the absence of

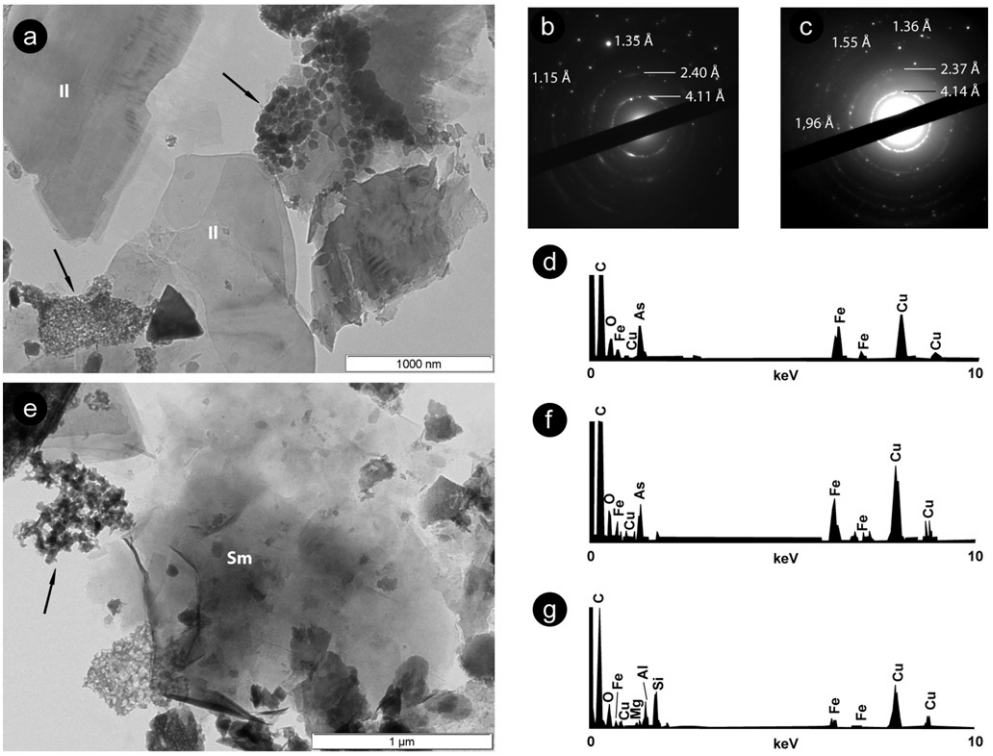

Fig. 8. TEM image from *Penedono* showing moiré-pattern on k-mica flakes, goethite spherical nanoparticles and clusters of nanoparticles with granular texture (arrows) (a); SAED patterns of spherical goethite (a–b) and granular clusters (a–c); EDS spectrum was obtained on the spherical nanoparticles (a–d); beidellite is associated with As–Fe rich clusters with irregular morphology (e); EDS spectra obtained on the upper cluster (arrow) (e–f) and on the beidellite platelets (e–g). Il = illite; Sm = smectite.

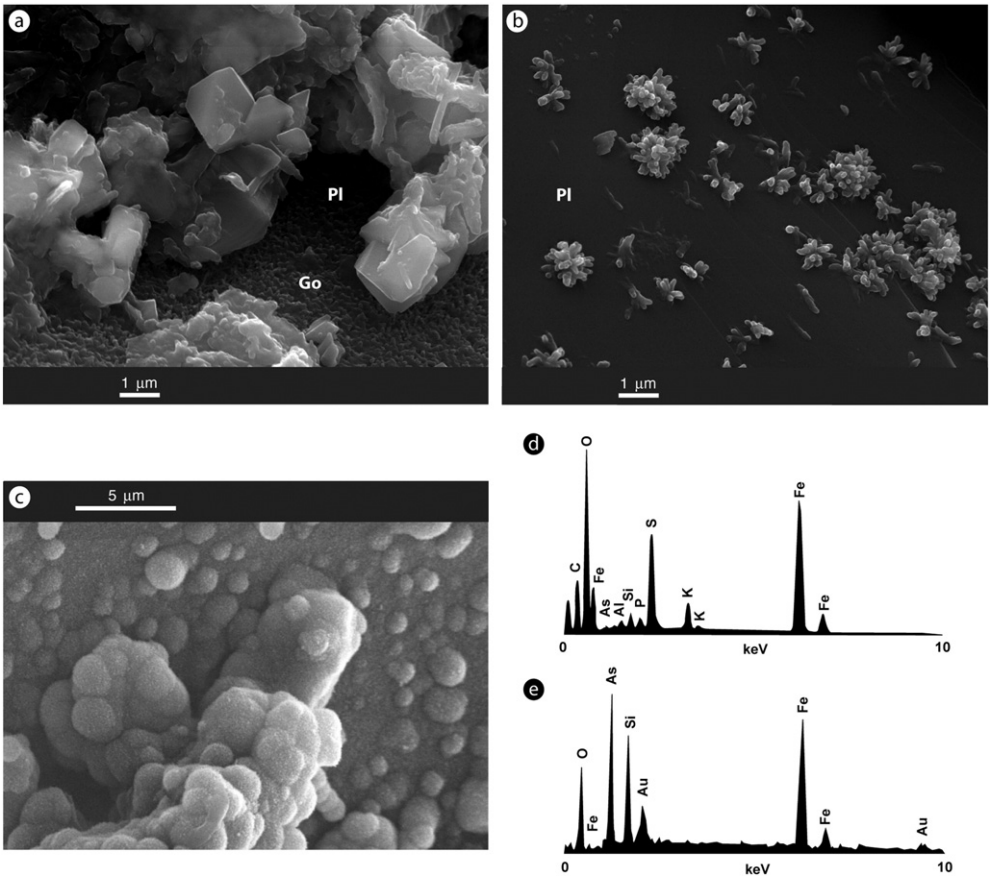

Fig. 9. FESEM images of *Cerdeirinha* sample with pseudocubic crystals of jarosite (a) and goethite (Go) coating plagioclase (Pl) surfaces (a–b); SEM image of *Penedono* sample with As–Fe-rich globular aggregates (c); EDS spectrum of jarosite (d); EDS spectrum of globular aggregates contaminated by silica (e).

vibration band at 630 cm^{-1} (Fig. 4a and b) and the presence of OH-stretching frequency at 3651 cm^{-1} (Fig. 4b) allowed this differentiation (Russell and Fraser, 1994). This later band was clearly the unique Al_2OH band identified in the beidellite structure (Kloprogge, 2006), since OH-stretching frequency at 3621 cm^{-1} of halloysite overlaps and obscures the second Al_2OH band (Fig. 4b). Therefore, despite the absence of a structural formula, the combination of SAED patterns, Greene-Kelly test and FTIR confirmed that the mineral species is beidellite.

The degree of disorder (XRD and SAED patterns) and the morphology features observed in TEM, such as diffuse and thin appearance, suggest that halloysite(7 Å) and beidellite are neoformed secondary minerals. They would have been formed by transformation of chlorite and mica, as reported by other authors for acidic conditions (Righi et al., 1999; Uzarowicz et al., 2011).

4.2. Jarosite and goethite

Jarosite ($KFe_3(SO_4)_2(OH)_6$) is the end member of the jarosite subgroup ($AFe_3(SO_4)_2(OH)_6$; A = K^+, Na^+, NH_4^+, H_3O^+, Pb^{2+},...). There can be several substitutions, but the most commonly found are between the hydronium ion H_3O^+, K^+ and Na^+ (Stoffregen et al., 2000; Figueiredo and Silva, 2011). Jarosite, formed as the result of the oxidation of sulfides, is one of the most relevant minerals in AMD environments due to its role as an acid generator in mine wastes (Desborough et al., 2010). Relevant reviews about their origin and properties, including stability, can be found in Alpers et al. (1989), Bigham (1994), Smith et al. (2006), and Stoffregen et al. (2000).

In the present study, jarosite was detected in the three sites, obeying to the following order of abundance: *Cerdeirinha* > *Lapa Grande* > *Penedono* (Table 3). The highest proportion in *Cerdeirinha* is in accordance with the chemical data presented in Table 1. In fact, *Cerdeirinha* samples pointed out the highest average values of Fe, S and K (17.6%, 1.76%, and 0.52% respectively, Table 1). In the three cases, it was only possible to identify the K-rich jarosite, which is known by its higher thermodynamic stability (Dutrizac and Jambor, 2000). Formation of natrojarosite or hydronium jarosite would imply very specific conditions, such as high rate Na:K and extremely rapid oxidation of sulfides. In such an acid environment, promoted by the sulfide oxidation, the K^+ ions required to form jarosite are provided by the partial dissolution of aluminosilicates, including the clay minerals. This is in agreement with the reported lack of alkalis in the beidellite composition.

In what morphology concerns, no significant differences were found in the jarosite of the three sites. The trigonal symmetry of jarosite comes reflected in the occurrence of well-defined hexagonal or pseudohexagonal crystals as found in TEM and FESEM study (Figs. 7 and 9a). The grain-size is always smaller than 15 nm and TEM results showed that most of the crystals have a size of <7 nm. Therefore, the observed grain-size is in the typical range reported in other studies for jarosite occurring in mine wastes (generally <20 nm, often <5 nm, Desborough et al., 2006, 2010).

Bigham (1994) and Stoffregen et al. (2000) present an overview of the equilibrium relations, namely of the stability relatively to iron oxides and oxyhydroxides. The association between jarosite and goethite (Fig. 9a) is in accordance with the equilibrium relations known for these two phases. In fact, the stability of jarosite in nature is mainly controlled by its transformation to goethite, in accordance with Eq. (3). This transformation is suggested by the textural relationship observed in Fig. 9a, including the presence of jarosite with corroded crystal edges. This dissolution should be favoured by dilution processes that are controlled by seasonal hydration/dehydration cycles.

$$KFe_3(SO_4)_2(OH)_{6(s)} \leftrightarrow 3FeO(OH)_s + K^+_{(aq)} + 2SO_4^{2-}(aq) + 3H^+_{(aq)} \quad (3)$$

The abundance of goethite (FeOOH) is also in agreement with the higher contents of Fe in *Cerdeirinha* and *Lapa Grande* (Table 1). In fact, this Fe-oxyhydroxide is more abundant in *Lapa Grande* (~12% in average) and *Cerdeirinha* (~10% in average), whereas is vestigial or absent at *Penedono* (Table 3).

Combining the chemical data (Table 1) with TEM and XRD analyses provides indication of the chemical nature of the goethite that is formed in the waste dumps. In fact, *Cerdeirinha* has the highest concentration of Al (6.00%) (Table 1). This result, associated with the EDS spectrum of goethite (Fig. 6c), suggests the presence of Al-goethite. Also, the d_{111} at 2.40 Å (Fig. 6b) is consistent with the Al substitution for Fe, as well as the XRD pattern proposed by Brindley and Brown (1980) for an aluminian goethite.

4.3. Amorphous As–Fe precipitates

The environmental fate and behaviour of amorphous As-rich precipitates may be influenced by a number of properties, such as size, state of aggregation, chemistry, and solubility, as observed by Silva et al. (2009) for Fe-nanominerals from coal-fired plants.

In the present study, the As-rich precipitates were seen to occur as spherical or granular aggregates. In *Penedono*, there are both morphologies, whereas *Lapa Grande* and *Cerdeirinha* have only spherical aggregates. Also, these precipitates were considerably more frequently observed in the *Penedono* samples, which is in agreement with the higher content of arsenic at this site (Table 1). Likewise, As:Fe ratio is higher in the nano-sized amorphous precipitates from *Penedono*. On the other hand, the presence of P was only detected in the *Lapa Grande* and *Cerdeirinha* precipitates. This composition is in accordance with the presence of mineralogical providers of P, such as apatite (Table 2). On the contrary, apatite is absent at *Penedono*, and consequently the concentration of P is lower (0.50%, Table 1).

Arsenic is an element of special environmental concern due to its high toxicity. It is especially abundant in the *Penedono* waste dump, with an average concentration of 7091 mg/kg (Table 1). However, in some particular samples, it reaches contents of up to more than 10,000 mg/kg. Moreover, Abreu et al. (2007) found arsenic concentrations of 40,000 mg/kg in the waste dumps.

Surface reactions, such as adsorption and coprecipitation on iron oxyhydroxides are known as relevant processes of controlling arsenic mobilization (Paktunc et al., 2008; Valente et al., 2012). Clay minerals (Goldberg, 2002; Dong, 2012) may also play important roles retaining arsenic in sulfide waste-dumps. Also, secondary soluble sulfates (e.g., melanterite) and hydroxysulfates (e.g., jarosite) may act as sinks for arsenic in AMD environments (Lottermoser and Ashley, 2006). Fe-oxyhydroxides can bind As (V), and jarosite can incorporate As(V) into its structure (Lu and Wang, 2012). In the present study, arsenic was detected in the composition of jarosite, as shown in Fig. 9d. Nevertheless, scorodite ($FeAsO_4 \cdot 2H_2O$) is the least soluble arsenate phase, responsible for controlling the mobilization of arsenic to pore waters in many mine waste systems (Langmuir et al., 2006). However, as stated by the previous authors, the ferric arsenates vary widely in stability, which has implication in the behaviour of arsenic in waste dumps.

The present study demonstrates the retention of arsenic by nano-sized amorphous precipitates, which may be a mineralogical precursor of the crystalline phase scorodite. This possibility is supported by the presence of scorodite in *Penedono*, where it occurs inside neoformed crusts (Fig. 10, not described in this study).

Previous thermodynamic studies indicate that in systems with high Fe:As molar ratio, completely crystalline scorodite was only formed at temperatures above 105 °C (Welham et al., 2000; Dutrizac and Jambor, 1988). At lower temperatures, some residual amorphous material remained. Such conditions may be occurring in *Cerdeirinha* and *Lapa Grande*, where earlier mineralogical studies indicate the absence of scorodite (Valente and Leal Gomes, 2009a). In contrast, for low molar Fe:As ratios (<1), Nishimura and Robins (1996) were able to form crystalline scorodite at 25 °C, through the evolution of an initially amorphous arsenate. So, similar process may be occurring at *Penedono*.

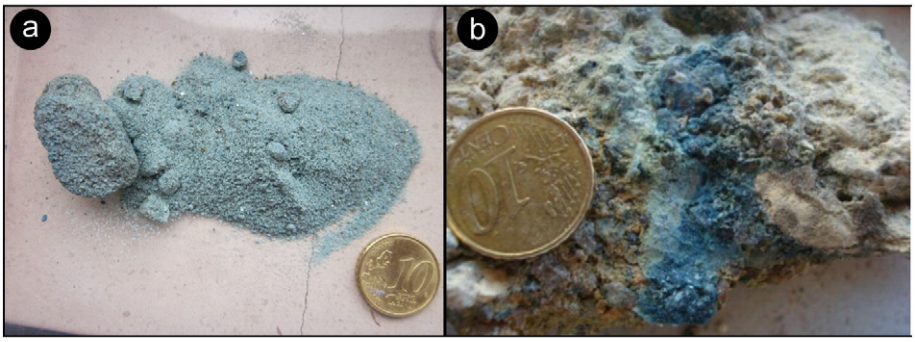

Fig. 10. Image of powder (a) and crustified (b) scorodite that occurs in the *Penedono* waste dump.

Depending on the ratio Fe:As, it is possible to assume the stability of amorphous ferric arsenates or its evolution to the crystalline phase, scorodite.

5. Conclusions

The study of the fine fraction (<2 μm) of mine wastes in three distinctive sulfide-rich waste dumps revealed that clay minerals (chlorite, illite, mica–vermiculite mixed-layer, halloysite(7 Å), and beidellite) occur in association with goethite, jarosite and Fe and As nanoprecipitates. Combination of analytical methods allowed to identify such phases and to describe their properties in such acidic conditions.

The results indicate that the three sites (*Cerdeirinha*, *Lapa Grande e Penedono*) present similar monotone clay mineral assemblage despite the differences in local geology and primary mineralogy. Also, acidity was seen to promote changes in composition and morphology of the clay minerals. As a consequence, EDS study reveals that beidellite has not a true chemical composition due to the lack of alkaline elements in its interlayer. Such alkaline elements, in particular potassium, are preferentially incorporated in jarosite. Moreover, the diffuse and thin appearance of the beidellite crystals may be produced by the acidity of the environment.

In addition to acidity, seasonal cycles of hydration–dehydration were pointed as responsible for morphological variations in the rolling of the of halloysite(7 Å) layers. Furthermore, these seasonal cycles may have influence on the equilibrium conditions that control the stability of secondary iron minerals. Dilution associated with rainfall may promote instability of jarosite, which was confirmed by the presence of corroded crystal edges observed in FESEM images. Nevertheless, jarosite is the dominant secondary mineral in the three sites, exhibiting well-defined euhedral habits. In turn, goethite appears as nano-size aggregates with acicular, needles and globular habits, always with low crystallinity. In terms of composition, it is an Al-rich goethite, which is in agreement with the high content of Al in the waste dumps.

The element that poses highest environmental concern is arsenic, especially in *Penedono* where the mine wastes have higher contents of this toxic element. Jarosite and aggregates of As–Fe-rich spherical nanoparticles were the main sinks of arsenic identified in the waste dumps. These aggregates are amorphous ferric arsenates, but in conditions of appropriate Fe:As ratio they may be a precursor of a crystalline arsenate, namely scorodite. So, this justifies the occurrence of this arsenate in *Penedono* where the Fe:As ratio is lower than at the other two sites.

The textural relationships detected among the small sized phases indicated that the amorphous As–Fe-rich nanoprecipitates are confined by the high external surface area of the clay mineral (beidellite). Additionally, the obtained results suggested that AMD conditions control the physical–chemical transformations, namely constraining the stability of the secondary phases. Acidity is responsible for the degradation of the clay minerals, which is reflected in their crystalochemistry, structural order–disorder and morphology. On the contrary, jarosite is more stable, being a dominant secondary mineral in such environmental conditions.

Acknowledgments

The authors thank António Azevedo for his help in XRD analysis and Elisabete Vivas for her assistance with the preparation of clay fraction. The research was funded by the national budget of the Portuguese Republic through FCT-Fundação para a Ciência e Tecnologia under the project PEst-OE/CTE/UI0697/2011. The authors are also grateful to the Editor and to an anonymous reviewer for their valuable comments and suggestions.

References

Abreu, M., Matias, M.J., Magalhães, M.F., Basto, M.J., 2007. Potencialites of *Pinus pinaster* and *Cytisus multiflorus* on the phytostabilization of the Santo António (Penedono) gold mine dumps. Rev. Ciências Agrár. 30, 335–349.

Alpers, C.N., Nordstrom, D.K., Ball, J.W., 1989. Solubility of jarosite solid solutions precipitated from acid mine waters, Iron Mountain, California, USA. Sci. Géol. Bull. 42, 281–298.

Alpers, C.N., Blowes, D.W., Nordstrom, D.K., Jambor, J.L., 2000. Secondary minerals and acid mine-water chemistry. In: Jambor, J.L., Blowes, D.W. (Eds.), Short Course Handbook on Environmental Geochemistry of Sulphide Mine-Waters. Mineral Assoc Can, pp. 247–270.

Bates, T.F., 1971. The kaolin minerals. In: Gard, J.A. (Ed.), The Electron-Optical Investigation of Clays. Monograph 3. Mineralogical Society, London, pp. 109–157.

Bigham, J.M., 1994. Mineralogy of ochre deposits formed by sulphide oxidation. In: Blowes, D.W., Jambor, J.L. (Eds.), The Environmental Geochemistry of Sulfide Mine-Wastes. Mineralogical Association of Canada Short Course Handbook 22, pp. 103–132.

Bigham, J.M., Nordstom, D.K., 2000. Iron and aluminum hydroxy-sulfates from acid sulfate waters. In: Alpers, C.N., Jambor, J.L., Nordstrom, D.K. (Eds.), Sulfate Minerals: Crystallography, Geochemistry, and Environmental Significance. Reviews in Mineralogy and Geochemistry 40, pp. 351–403.

Bishop, J.L., Murad, E., 2005. The visible and infrared spectral properties of jarosite and alunite. Am. Mineral. 90, 1100–1107.

Brindley, G.W., 1980. Quantitative X-ray mineral analysis of clays. In: Brown, G., Brindley, G.W. (Eds.), Crystal Structures of Clay Minerals and Their X-Ray Identification. Monograph No. 5. Mineralogical Society, London, pp. 411–438.

Brindley, J.W., Brown, G., 1980. Crystal Structure of Clay Minerals and their X-ray Identification. Monograph 5. Mineralogical Society, London (495 pp.).

Desborough, G.A., Smith, K.S., Lowers, H.A., Swayze, G.A., Hammarstrom, J.M., Diehl, S.F., Driscoll, R.L., Leinz, R.W., 2006. The use of synthetic jarosite as an analog for natural jarosite. Proceedings of the Seventh International Conference on Acid Rock Drainage. St. Louis, Missouri, pp. 458–475.

Desborough, G.A., Smith, K.S., Lowers, H.A., Swayze, G.A., Hammarstrom, J.M., Diehl, S.F., Leinz, R.W., Driscoll, R.L., 2010. Mineralogical and chemical characteristics of some natural jarosites. Geochim. Cosmochim. Acta 74, 1041–1056.

Dill, H.G., Kaufhold, S., Dohrmann, R., 2011. A late-stage hydrothermal phosphate-bearing montmorillonite argilitization from the tourmaline-bearing pegmatite of Alto dos Quintos Mine, northeast Brazil. Clay Miner. 46, 473–485.

Dong, H., 2012. Clay–microbe interactions and implications for environmental mitigation. Elements 8, 113–118.

Dutrizac, J., Jambor, J., 1988. The synthesis of crystalline scorodite $FeAsO_4$ $2H_2O$. Hydrometallurgy 19, 377–384.

Dutrizac, J.E., Jambor, J.L., 2000. Jarosites and their application in hydrometallurgy. Rev. Mineral. Geochem. 40, 405–452.

Figueiredo, M., Silva, T., 2011. The positive environmental contribution of jarosite by retaining lead in acid mine drainage areas. Int. J. Environ. Res. Public Health 8, 1575–1582.

Galan, E., Carretero, M., Fernandez-Caliani, J., 1999. Effects of acid mine drainage on clay minerals suspended in the Tinto River (Rio Tinto, Spain). An experimental approach. Clay Miner. 34, 99–108.
Goldberg, S., 2002. Competitive adsorption of arsenate and arsenite on oxides and clay minerals. Soil Sci. Soc. Am. J. 66, 413–421.
Gomes, P., Valente, T., Pamplona, J., Sequeira Braga, M.A., Pissarra, J., Grande, J.A., 2013. Metal uptake by native plants and revegetation potential of mining sulfide-rich waste-dumps. J. Phytoremediat. http://dx.doi.org/10.1080/15226514.2013.810586.
Grande, J.A., de la Torre, M.L., Cerón, J.C., Beltrán, R., Gómez, T., 2010. Overall hydrochemical characterization of the Iberian Pyrite Belt. Main acid mine drainage generating sources (Huelva, SW Spain). J. Hydrol. 390, 123–130.
Greene-Kelly, R., 1952. Irreversible dehydration in montrnorillonite. Clay Mineral Bull. 1, 221–227.
Greene-Kelly, R., 1953. Irreversible dehydration in montmorillonite. Part II. Clay Mineral Bull. 1, 52–56.
Hammarstrom, J.M., Seal II, R.R., Meier, A.L., Jackson, J.C., 2003. Weathering of sulfidic shale and copper mine waste: secondary minerals and metal cycling in Great Smoky Mountains National Park, Tennessee, and North Carolina, USA. Environ. Geol. 43, 35–57.
Henning, K.H., Störr, M., 1986. Electron Micrographs (TEM, SEM) of Clays and Clay Minerals, Akademie — Verlag Berlin (Schriftenreihe für geologische Wissenschaften, Bd. 25). p. 352.
Hoffert, J.R., 1947. Acid mine drainage. Ind. Eng. Chem. 39 (5), 642–646.
Kloprogge, J.T., 2006. Spectroscopic studies of synthetic and natural beidellites: a review. Appl. Clay Sci. 31, 165–179.
Landers, M., Gilkes, R.J., Wells, M.A., 2009. Rapid dehydroxylation of nickeliferous goethite in lateritic niquel ore: X-ray diffraction and TEM investigation. Clay Clay Miner. 57 (6), 751–770.
Langmuir, D., Mahonoy, J., Rowson, J., 2006. Solubility products of amorphous ferric arsenate and crystalline scorodite ($FeAsO_4[.]2H_2O$) and their application to arsenic behaviour in buried mine tailings. Geochim. Cosmochim. Acta 70, 2942–2956.
Lottermoser, B.G., Ashley, P., 2006. Mobility and retention of trace elements in hardpan-cemented cassiterite tailings, north Queensland, Australia. Environ. Geol. 50, 835–846.
Lu, X., Wang, H., 2012. Microbial oxidation of sulfide tailings and the environmental consequences. Elements 8, 119–124.
Moore, D.M., Reynolds Jr., R.C., 1997. X-Ray Diffraction and the Identification and Analysis of Clay Minerals. Oxford University Press, New York (378 pp.).
Murad, E., Rojík, P., 2003. Iron-rich precipitates in a mine drainage environment: influence of pH on mineralogy. Am. Mineral. 88, 1915–1918.
Nishimura, T., Robins, R.G., 1996. Crystalline phases in the system Fe(III)–As(V)–H_2O at 25 °C. In: Dutrizac, J.E., Harris, G.B. (Eds.), Iron Control and Disposal. Proceedings of the 2nd International Symposium on Iron Control in Hydrometallurgy, Ottawa, Canada, October, 20–23, 1996, pp. 521–533.
Paktunc, D., Dutrizac, J., Gertsman, V., 2008. Synthesis and phase transformations involving scorodite, ferric arsenate and arsenical ferrihydrite: implications for arsenic mobility. Geochim. Cosmochim. Acta 72, 2649–2672.
Plathe, K.L., von der Kammer, F., Hassellöv, M., Moore, J.N., Murayama, M., Hofmann, T., Hochella Jr., M.F., 2013. The role of nanominerals and mineral nanoparticles in the transport of toxic trace metals: field-flow fractionation and analytical TEM analyses after nanoparticle isolation and density separation. Geochim. Cosmochim. Acta 102, 213–225.
Ribeiro, J., Flores, D., Ward, C., Silva, L., 2010. Identification of nanominerals and nanoparticles in burning coal waste piles from Portugal. Sci. Total Environ. 408, 6032–6041.
Righi, D., Huber, K., Keller, C., 1999. Clay formation and podzol development from postglacial moraines in Switzerland. Clay Miner. 34, 319–332.
Russell, J.D., Fraser, A.R., 1994. In: Wilson, M.J. (Ed.), Clay Mineralogy: Spectroscopic and Chemical Determinative Methods. Chapman & Hall, London, UK.
Silva, M.V., Neiva, A.M., 1990. Geochemistry of the granites and their minerals from Paredes da Beira-Penedono, Northern Portugal. Chem. Geol. 85, 147–170.
Silva, L., Moreno, T., Querol, X., 2009. An introductory TEM study of Fe-nanominerals within coal fly ash. Sci. Total Environ. 407, 4972–4974.
Smith, A.M.L., Hudson-Edwards, K.A., Dubbin, W.E., Wright, K., 2006. Dissolution of jarosite [KFe3(SO4)2(OH)6] at pH 2 and 8: insights from batch experiments and computational modelling. Geochim. Cosmochim. Acta 70, 608–621.
Stoffregen, R.E., Alpers, C.N., Jambor, J.L., 2000. Alunite–jarosite crystallography, thermodynamics, and geochronology. In: Alpers, C.N., Jambor, J.L., Nordstrom, D.K. (Eds.), Sulfate Minerals: Crystallography, Geochemistry, and Environmental Significance. Reviews in Mineralogy and Geochemistry 40. Mineralogical Society of America, Washington, D.C., pp. 453–479.
Uzarowicz, L., Skiba, S., Skiba, M., Michalik, M., 2011. Clay-mineral formation in soils developed in the weathering zone of pyrite-bearing schists: a case study from the abandoned pyrite mine in Wieściszowice, Lower Silesia, SW Poland. Clays Clay Minerals 59, 581–594.
Valente, T., Leal Gomes, C., 2007. The role of two acidophilic algae as ecological indicators of acid mine drainage sites. J. Iber. Geol. 33, 283–294.
Valente, T., Leal Gomes, C., 2009a. Occurrence, properties and pollution potential of environmental minerals in acid mine drainage. Sci. Total Environ. 407, 1135–1152.
Valente, T., Leal Gomes, C., 2009b. Fuzzy modelling of acid mine drainage environments using geochemical, ecological and mineralogical indicators. Environ. Geol. 57, 653–663.
Valente, T., Antunes, M.D., Sequeira Braga, M.A., Pamplona, J.M., 2011. Geochemistry and mineralogy of ochre-precipitates formed as waste products of passive mine water treatment. Geochem. Explor. Environ. Anal. 11, 103–106.
Valente, T., Antunes, M., Sequeira Braga, M.A., Prudêncio, M.I., Marques, R., Pamplona, J., 2012. Mineralogical attenuation for metallic remediation in a passive system for mine water treatment. Environ. Earth Sci. http://dx.doi.org/10.1007/s12665-011-1205-7.
Valente, T., Grande, J.A., de la Torre, M.L., Santisteban, M., Cerón, J.C., 2014. Mineralogy and environmental relevance of AMD-precipitates from the Tharsis mines, Iberian Pyrite Belt (SW, Spain). Appl. Geochem. 39, 11–25.
Valsami-Jones, E., 2000. Section 3: minerals in contaminated environments. In: Campbell, L.S., Valsami-Jones, E., Batchelder, M. (Eds.), Environmental Mineralogy: Microbial Interactions, Anthropogenic Influences, Contaminated Land and Waste. The Mineralogical Society Series vol.9, pp. 201–205.
Vazquez, O., Monnell, J.D., Pu, X., Neufeld, R.D., 2011. Major processes dominating the release of aluminum from smectite clays when leached with acid mine drainage. Environ. Eng. Sci. 28 (3).
Waychunas, G., Kim, C., Banfield, J., 2005. Nanoparticulate iron oxide minerals in soils and sediments: unique properties and contaminant scavenging mechanisms. J. Nanoparticle Res. 7, 409–433.
Welham, N.J., Malatt, K.A., Vukcevic, S., 2000. The stability of iron phases presently used for disposal from metallurgical systems a review. Miner. Eng. 13 (8–9), 911–931.
Wilke, B., 2005. Determination of chemical and physical soil properties. In: Margesin, R., Schinner, F. (Eds.), Manual of Soil Analysis. Springer, pp. 47–96.